AIAA JOURNAL
Vol. 37, No. 1, January 1999

Normal Vortex Interaction with a Circular Cylinder

S. Krishnamoorthy,* A. A. Gossler,* and J. S. Marshall†
University of Iowa, Iowa City, Iowa 52242

Interaction of a columnar vortex with a long circular cylinder translated normal to the vortex axis is examined for the case where the cylinder diameter is much larger than the vortex core radius. The study focuses on understanding and quantifying the limitations of traditional vortex filament models arising from vortex-induced separation of the cylinder boundary layer and vortex core shape deformation. These limitations are examined over a wide range of values of the impact parameter, defined as the ratio of the ambient normal velocity past the cylinder to the maximum vortex azimuthal velocity. Filament model predictions of vortex displacement are compared to experimental data both before and after vortex-induced boundary-layer separation. Experimental data are presented showing the importance of the ambient normal velocity to the cylinder in delaying vortex-induced boundary-layer separation, so that for cases with high impact parameter the flow is governed by inviscid effects even as the vortex moves quite close to the cylinder surface. The inviscid shape deformation of the vortex core is modest in the cases examined, even for close vortex–cylinder interaction, and is shown to have small effect on the surface pressure. The topology of secondary vorticity structures ejected from the cylinder boundary layer is examined using a two-color laser-induced fluorescence technique and is found to be qualitatively different for cases with high and low values of the impact parameter.

I. Introduction

VORTEX interaction with solid bodies is of importance in a wide variety of fluid flow problems, including aircraft wake interaction with following aircraft, turbine performance and wear, dynamic stall processes, and control surface juncture vortices. Particularly important applications occur in the area of helicopter interactional aerodynamics, in which a variety of vortex–body interactional processes are known to affect vehicle performance.[1,2] The specific flow examined in this paper is that of an initially columnar vortex impinging upon a circular cylinder, which is representative of aspects of the problem of interaction of rotor wake vortices with a helicopter fuselage or empennage.

General reviews of vortex–body and vortex–wall interactions are given by Rockwell[3] and Doligalski et al.,[4] and a review of vortex–cylinder interaction in particular is given by Kim and Komerath.[5] Several previous experimental studies of vortex–cylinder interaction have been performed that report information such as vortex trajectory prior to impact with the cylinder and surface pressure variation on the cylinder.[6–9] Bi et al.[7] note that tip vortex impingement on a cylinder causes large transient loads on the surface coupled with an adverse pressure gradient in the spanwise direction, suggesting separation of the boundary layer at the cylinder leading edge. Brand et al.[9] note that interaction with a cylinder appears to induce breakdown of an impinging vortex and that following impingement the vortex breaks into two separate parts, which travel independently past the sides of the cylinder while a weak low-pressure region remains at the point of impingement. Liou et al.[6] present phase-averaged laser Doppler velocimetry and surface pressure data that show that surface pressure measurements deviate from potential flow predictions well before the vortex impinges on the cylinder. They further suggest that these deviations from potential theory are associated with shedding of secondary vorticity from the cylinder.

A computational study of inviscid vortex bending as it approaches a cylinder is reported by Affes and Conlisk[10] using vortex filament theory. The filament theory predictions for surface pressure along the cylinder leading edge and for vortex trajectory are found to compare well with experimental data until the vortex comes to within a distance of about a core radius from the cylinder leading edge for the specific cases examined.[11] Computations of vortex–cylinder interaction using an extended formulation of vortex filament theory that accounts for core radius variation due to axial stretching are reported by Marshall and Yalamanchili.[12] Computations of the boundary-layer response on a cylinder in the vicinity of a vortex are reported by Affes et al.[13] and Xiao et al.,[14] where the vortex-induced pressure gradient tangent to the body is obtained by the filament theory predictions. Comparisons of boundary-layer computations with experimental results are given by Affes et al.[15] These computations indicate that the vortex-induced velocity field induces ejection of a tongue-like region of vorticity along the cylinder leading edge. These studies solve the boundary-layer equations instead of the full Navier–Stokes equations, and the computations must be stopped at the point of boundary-layer separation.

In a study of vortex interaction with a thin blade, Krishnamoorthy and Marshall[16] report on the geometry of the secondary vorticity field shed from the blade and its interaction with the primary vortex. When the maximum swirl velocity of the vortex is sufficiently large compared to the blade translation speed, the vorticity ejected from the blade leading edge due to the vortex-induced flow forms a series of discrete vortex loops that are attached at different positions along the blade span. The loops wrap around the outer surface of the primary vortex core and spread both upstream and downstream along the vortex axis. The secondary vortex loops induce core deformation, axial wave formation, and ejection of vorticity from the primary vortex.

The current paper examines the limitations of vortex filament models for prediction of vortex–cylinder interaction arising from separation of the cylinder boundary layer and inviscid deformation of the vortex core shape. The paper particularly focuses on the effect of the impact parameter, defined as the ratio of the cylinder translation velocity to the maximum vortex azimuthal velocity, on the cylinder viscous response. The first specific objective of the paper is to report experimental data showing the effect of cylinder normal velocity on onset of vortex-induced boundary-layer separation over a range of values of the impact parameter. These data supplement computational results of Xiao et al.,[14] which are obtained for the case of zero normal ambient velocity. A second objective is to examine the error incurred by applying inviscid vortex filament prediction methods for cases where the vortex is sufficiently close to the cylinder that either significant core shape deformation or boundary-layer separation has occurred. A third objective is to examine the topological form of the separated secondary vortex structures as they are advected away from the cylinder and interact with the primary vortex. This study complements that of Affes et al.,[15] which focuses on the initial ejection of vorticity from the cylinder boundary layer.

Received Jan. 27, 1998; revision received Aug. 10, 1998; accepted for publication Sept. 16, 1998.

*Graduate Research Assistant, Iowa Institute of Hydraulic Research.
†Associate Professor, Department of Mechanical Engineering and Research Engineer, Iowa Institute of Hydraulic Research.

The experimental setup and procedure are described in Sec. II. Section III presents parametric data for onset of vortex-induced boundary-layer separation from the cylinder leading edge and compares experimental and computational results for displacement of the vortex axis before and after separation. Section IV examines the effect of vortex core shape deformation on the cylinder surface pressure distribution by comparing computations performed with the vortex filament method and with the full Euler equations. The topological form of the secondary vorticity shed from the cylinder and its dependence on the system governing parameters are discussed in Sec. V. Conclusions are given in Sec. VI.

II. Experimental Setup

In the experiments, a circular cylinder with horizontal axis is translated through a vertical intake vortex with a downward axial flow (Fig. 1). The towing speed U of the cylinder is set by a computer-controlled screw drive to minimize vibrations and maintain a constant towing speed. The primary vortex is generated in water in a cylindrical inner tank (30-cm diameter), about which is placed an outer rectangular tank (101×43 cm cross section and 123 cm high) that houses the cylinder and support arms of the tow carriage. Water is circulated through the system via tangential inlet jets at the top of the inner cylindrical tank and an outlet orifice at the tank bottom. The intake vortex is trapped at the top of the cylindrical tank by an inverted funnel, which both stabilizes the vortex and increases the core radius.

There is a 13-cm-wide gap in the inner cylindrical tank to allow passage of the cylinder. To avoid possible oscillations of the vortex, the gap is closed by clear 1-cm-wide flexible plastic strips, extending both downward from above the gap and upward from below the gap. The cylinder pushes these strips out of the way during passage through the gap; however, the strips are sufficiently far from the vortex that their motion during body passage is observed to have no significant effect on the vortex.

The circular cylinder used for study of vortex–cylinder interaction has diameter $D = 8.9$ cm and span length $b = 34$ cm. A staggered array of 25 spanwise dye ports (0.34-mm diameter) in two rows centered along the cylinder span is used for injection of dye into the cylinder boundary layer. The two dye port rows are placed with one just above the cylinder leading edge and the other just below the cylinder leading edge. The dye ports in these rows are separated by a distance of 13 mm, and the rows are separated from each other by a distance of 6.5 mm. The lateral sides of the cylinder are supported outside of the inner cylindrical tank, such that the tip vortices do not influence the interaction.

The laser-induced fluorescence (LIF) technique is used for flow visualization with dyes that fluoresce at two different colors. The primary vortex is visualized using dye that fluoresces red (Sulfurhodamine 640), and the cylinder boundary layer is visualized with dye that fluoresces yellow (Rhodamine chloride 590) when exposed to light with wavelength in the range 500–600 nm. The dyes are excited by a laser sheet formed from the green line of a continuous argon ion laser (with wavelength in the range 457–514 nm). Photographs are taken using both a 35-mm still camera and a standard video camera, with frame rates of approximately 4 and 30 frames/s, respectively. The green laser light is filtered out so that only the emitted light of the dyes is recorded on film. The orientation of the vertical and horizontal planes used for flow visualization, labeled A and B, respectively, is shown in Fig. 1. In the experiments, the vertical plane A is displaced along the cylinder span some distance ahead of the ambient vortex axis (as indicated in the text) to account for spanwise bending of the vortex during the interaction.

The yellow dye is gravity fed into the cylinder boundary layer from an external reservoir. The flow rate of yellow dye can be finely controlled by adjusting both the gravity head of the reservoir and a needle valve placed in the feed line. Experiments were performed without the vortex present to ensure that the injection of yellow dye does not disturb the cylinder boundary layer. Red dye is fed continuously into the primary vortex within the inverted funnel at the top of the inner cylindrical tank during the experiments and carried downward by the ambient axial flow within the vortex core. In the current paper, the LIF photographs have been digitally processed to insert the cylinder profile and to change the colored dyes to gray scale, such that the boundary-layer fluid appears darker than the dyed fluid within the primary vortex.

The azimuthal velocity field within and outside the vortex core is measured by a particle-image velocimetry (PIV) system, which uses a double-pulsed Nd: YAG laser synchronized with a charge-couple device camera (1317×1035 pixels). Data processing is performed using autocorrelation with the TSI Insight software. The PIV data are obtained with a spacing of about 1 mm between vectors and 50% overlap of interrogation regions. Neutrally buoyant polycrystalline particles are used for flow seeding, with specific gravity 1.00 ± 0.02 and more than 90% of the particle diameters less than 10 μm. The seed particles are formed into a milky suspension that is injected into the flow through the inverted funnel at the top of the inner cylindrical tank. PIV images are acquired after the particles have dispersed thoroughly within the test region. The PIV data (circular symbols in Fig. 2) have a root-mean-square scatter about the best-fit curve (solid line) of 3.6% of the maximum azimuthal velocity. The core radius σ_0 is set equal to the value of r at which the best-fit curve has a maximum, and the circulation Γ is obtained by fitting the expression $\Gamma/2\pi r$ for azimuthal velocity from a line vortex to the measured data for large values of r.

The axial velocity profile $w(r)$ of the intake vortex is measured by photographing the motion of a large number of small (0.5–1-mm diameter) neutrally buoyant immiscible dye globules (bromobenzene and paraffin oil mixed with a fat soluble dye), which are released through a hypodermic needle at the top of the tank and carried

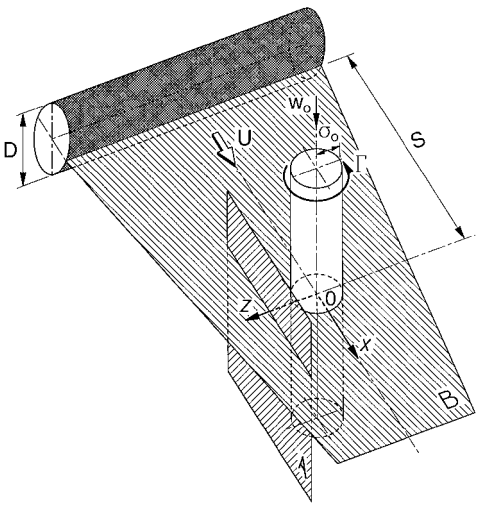

Fig. 1 Coordinate system used to measure vortex displacement, various parameters that govern normal vortex-cylinder interaction, and the vertical plane A and horizontal plane B used for flow visualization.

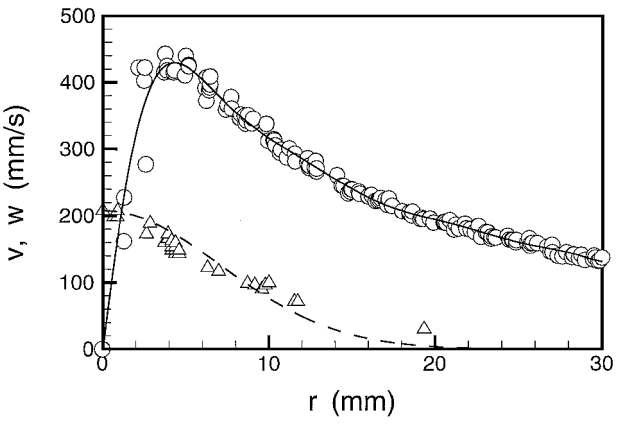

Fig. 2 Experimental data for azimuthal velocity (○) and axial velocity (△) of the primary vortex as a function of radial distance from the center of the inner cylindrical tank; best-fit curves are plotted for the azimuthal velocity (——) and axial velocity (– – –).

downward by the vortex axial flow. The measured axial velocity profile is well fit by a Gaussian function of the form

$$w(r) = w_{\max} \exp\left(-r^2/\sigma_1^2\right) \tag{1}$$

where σ_1 is another measure of the vortex core radius and $w_{\max}$ is the axial velocity on the vortex centerline. The axial velocity data (triangular symbols in Fig. 2) have a root-mean-square scatter about the fit (1) (dashed curve) of 8.3% of $w_{\max}$. The average axial velocity over the core radius w_0 is defined by

$$w_0 = \frac{2}{\sigma_1^2}\int_0^{\sigma_1} r\,w(r)\,\mathrm{d}r \cong 0.63 w_{\max} \tag{2}$$

For all experiments reported, the primary vortex is held in a fixed state. The measures σ_0 and σ_1 of the vortex core radius are $\sigma_0 = 4.0 \pm 1.0$ mm and $\sigma_1 = 10 \pm 2$ mm, based on the azimuthal and axial velocity components, respectively. The maximum axial velocity is $w_{\max} = 208 \pm 20$ mm/s, and the average axial velocity is $w_0 = 131 \pm 15$ mm/s. The vortex circulation is $\Gamma = 24 \times 10^3 \pm 1 \times 10^3$ mm^2/s. The towing velocity U is varied from 25 to 300 mm/s.

Normal vortex–cylinder interaction is governed by four dimensionless parameters: the impact parameter $I \equiv 2\pi\sigma_0 U/\Gamma$, the thickness parameter $T \equiv D/\sigma_0$, the vortex Reynolds number $Re_v \equiv \Gamma/\nu$ (where ν is the kinematic viscosity), and the axial flow parameter $A \equiv 2\pi\sigma_0 w_0/\Gamma$. The cylinder Reynolds number Re_c can be expressed in terms of these parameters as $Re_c = Re_v T I/2\pi$. The value of the axial flow parameter is $A = 0.14 \pm 0.06$, which indicates that the vortex used in the experiments is in a subcritical state (so that waves of variable core area can propagate both upstream and downstream on the vortex core). The vortex Reynolds number is $Re_V = 2.5 \times 10^4$. The thickness ratio is held fixed at $T = 22.3$. Experiments are performed for values of the impact parameter ranging over the interval $0.027 \le I \le 0.32$ at intervals of $\Delta I = 0.027$. The cylinder Reynolds number correspondingly varies over the interval $2.4 \times 10^3 \le Re_c \le 2.8 \times 10^4$. Experimental results often are shown here only for two specific cases with $I = 0.027$ and 0.21, which are representative of the flow behavior at low and high values of the impact parameter, respectively.

III. Vortex Displacement and Boundary-Layer Separation

A comparison by Affes et al.[11] of filament model predictions with experimental results reports good agreement in vortex position and cylinder surface pressure until the vortex approaches to within a distance on the order of the core diameter from the cylinder leading edge. After this point, the sharp spike in surface pressure predicted by the filament model near the point of vortex impact is observed to be smoother and less pronounced in the experimental data. This disagreement can seriously degrade the accuracy of the vortex filament model in predicting maximum vortex-induced force for problems involving close vortex–body interaction. The objectives of the present section are to expand the evaluation of filament model predictions for cases with very different values of the impact parameter and to specifically examine how degradation in filament model predictions is correlated with boundary-layer separation from the cylinder leading edge.

Experimental data are obtained by analysis of video pictures of LIF images in the horizontal B plane at a frequency of 30 Hz. Boundary-layer separation from the cylinder leading edge is detected by observation of ejection of the yellow dyed fluid in the horizontal plane. The data are compared to numerical predictions obtained using a combination of a vortex filament model and a source panel method[17] to represent the cylinder. The numerical method used for evolution of the vortex filament is similar to the thin tube model of Knio and Ghoniem.[18] In this model, the vorticity is interpolated along the filament using a series of blob-like vorticity elements. In the current calculations, Gaussian blobs are used with a radial length scale of σ_0. The vortex-induced velocity is computed by direct integration over the vortex blobs. The blob amplitudes vary in proportion to the local stretch of the vortex filament, and the vortex core radius is assumed to remain constant.

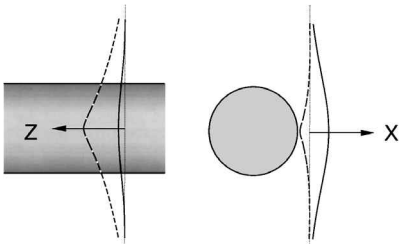

Fig. 3 Predictions for vortex displacement in the chordwise and spanwise directions, shown for cases with $I = 0.21$ (——) and 0.027 (– – –) for cylinder position $S/\sigma_0 = -3.4$.

The vortex filament is resolved over an axial length of $50\sigma_0$ with 400 vortex blobs. The cylinder has diameter $22.3\sigma_0$, which is the same diameter as used in the experiments. The vortex is initially located a distance $30\sigma_0$ from the cylinder leading edge, and 1000 source panels are initially used to discretize the cylinder over a span length of $80\sigma_0$. The panel resolution is increased as the vortex approaches the cylinder, so that the spanwise panel spacing near the point of vortex impact is less than 20% of the nearest vortex–cylinder separation distance as the vortex approaches to a distance σ_0 from the cylinder. Both ends of the computed section of the vortex filament are connected to semi-infinite straight filaments. Similarly, both ends of the computed section of the cylinder are connected to semi-infinite cylinders, on which the source sheet strength is set based on the potential flow solution for two-dimensional uniform flow past a cylinder. Time advancement is performed using a second-order Adams–Bashforth scheme, with time step held fixed at $\Delta t = 0.6\sigma_0^2/\Gamma$.

The three-dimensional form of the predicted vortex displacement is shown for cases with high and low values (0.21 and 0.027) of the impact parameter in Fig. 3 at a given cylinder position. The spanwise displacement increases with decrease in impact parameter because the vortex has a longer time to respond to the velocity induced by its image with slower cylinder translation velocities. The chordwise displacement is determined by two opposing effects: the velocity directed away from the cylinder induced by the motion of the body and the velocity directed toward the cylinder caused by the self-induced velocity of the vortex arising from the spanwise displacement. For high impact parameters, the first of these effects dominates, and the vortex is repelled from the cylinder by an amount that increases with increase in cylinder translation speed. For low impact parameters, the vortex self-induced velocity dominates, and the vortex appears to be attracted to the cylinder.

The displacement of the centroid of the vortex cross section in the horizontal plane B in the chordwise and spanwise directions, denoted by X and Z, respectively, is plotted in Fig. 4 as a function of the cylinder leading-edge position S (relative to the initial vortex position). Filament model predictions are plotted for four different values of the impact parameter, and experimental data are plotted for cases with $I = 0.21$ (open symbols) and $I = 0.027$ (gray closed symbols). S is initially negative as the cylinder approaches the vortex and becomes positive as the cylinder passes through the initial vortex location. Data points prior to boundary-layer separation are represented by circles, and those obtained following separation are represented by triangles. The final triangular data point is close to the time at which the vortex breaks up. Sensitivity of the filament computations to selection of time step and spatial resolution was tested by repeating a case with impact parameter $I = 0.21$ with half as many vorticity control points and source panels and twice the time step ($\Delta t = 1.2\sigma_0^2/\Gamma$). The maximum vortex deflection distance in this test calculation is found to be within 0.03% of that in the reported computation for S/σ_0 between -30 and 0 and within 0.6% as S/σ_0 varies from 0 to 10.

For the high impact parameter case ($I = 0.21$), the vortex exhibits substantial bending, core deformation, and stretching as it wraps around the cylinder prior to boundary-layer separation. The boundary layer separates from the cylinder surface at a time when the cylinder leading edge has passed entirely through the vortex initial position ($S/\sigma_0 = 6$) and the vortex has become displaced in the

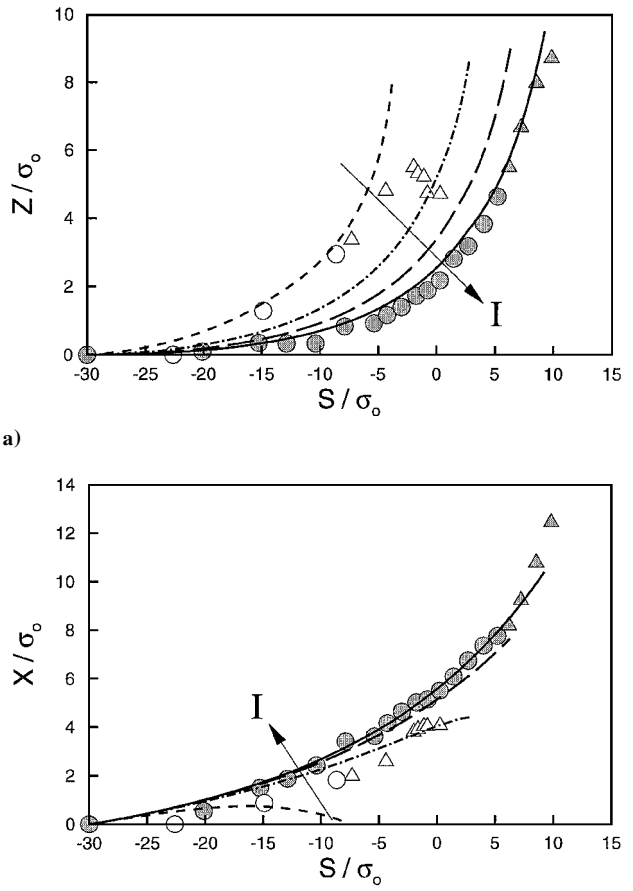

Fig. 4 Model predictions with $I = 0.21$ (——), 0.15 (– – –), 0.088 (– · –), and 0.027 (- - - -) and for experimental data with $I = 0.21$ (open symbols) and 0.027 (shaded symbols); experimental data points are given for times both before (circles) and after (triangles) boundary-layer separation from the cylinder. Displacement of vortex cross section in horizontal plane B: a) spanwise Z and b) chordwise X.

chordwise direction by a distance of about $8\sigma_0$. Following boundary-layer separation ($6 < S/\sigma_0 < 10$), the chordwise displacement continues to increase until the vortex breaks up at about $S/\sigma_0 = 12$. The inviscid filament model predictions agree well with the experimental data for both chordwise and spanwise vortex displacement, and the data following separation continue the trend of the inviscid predictions up to the point of vortex breakup.

The magnitude of vortex core area reduction due to axial stretching for the case with $I = 0.21$ is assessed by digitizing select video frames, where the area of the red dye patch covering the vortex cross section in the horizontal plane is determined using a commercially available image measurement and analysis software package (Sigma Scan Pro®). Red dye is gravity fed into the primary vortex at a constant rate during the interaction, so that the reduction in dye area is proportional to the reduction in vortex core area. The vortex core area is observed to reduce to about 70% of its initial value due to axial stretching just before the cylinder boundary layer separates. As explained by Marshall and Yalamanchili,[12] the core area reduction occurs as a result of a balance between axial stretching associated with vortex displacement and an axial velocity within the vortex core that arises from the axial variation in core area and acts to increase the core area near the cylinder.

For the low impact parameter case ($I = 0.027$), boundary-layer separation occurs at $S/\sigma_0 = -8$, while the cylinder is still almost one cylinder radius away from the vortex initial position. At the time of separation, the vortex displacement is only about $2\sigma_0$ in the chordwise direction and $3\sigma_0$ in the spanwise direction. The filament model predictions for the spanwise vortex displacement agree well with experimental data before separation but quickly deviate from the data following separation. This discrepancy is caused by the induced velocity from the secondary vortex structures, as discussed

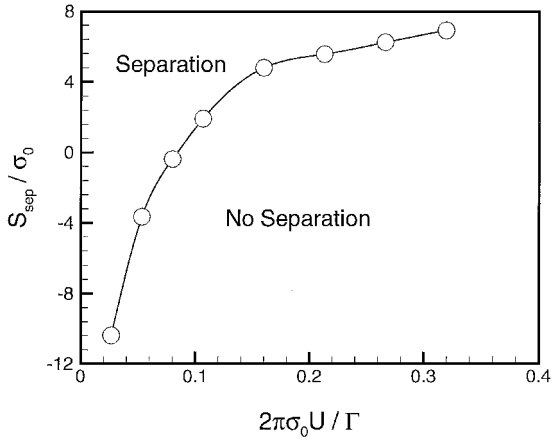

Fig. 5 Experimental data for the variation of the critical value of the cylinder leading edge position at the instant of boundary-layer separation S_{sep} as a function of impact parameter.

further in Sec. V. The filament model predictions for chordwise displacement for the $I = 0.027$ case indicate vortex attraction to the cylinder, whereas the corresponding experimental data for this case indicate vortex repulsion from the cylinder. This discrepency is believed to be a consequence of the high degree of sensitivity of the chordwise displacement to the impact parameter in the range $0.02 < I < 0.06$, as exhibited by the filament model predictions in Fig. 4b.

Experimental data for the critical value S_{sep} of the cylinder leading-edge position at the point of boundary-layer separation are given in Fig. 5 for different values of the impact parameter. For low values of impact parameter ($I < 0.08$), the slope of the critical curve in Fig. 5 is very high, such that S_{sep}/σ_0 is a large negative number as the impact parameter becomes very small. For this case, boundary-layer separation occurs when the cylinder is still quite far from the vortex. For values of the impact parameter larger than about 0.2, the slope of the critical curve becomes small, and the cylinder position at separation changes only slightly with increase in impact parameter. This effect is caused by the inviscid displacement of the vortex in the chordwise direction tending to maintain a nearly constant separation distance between the vortex and the cylinder leading edge after the cylinder has passed through the vortex initial position.[12]

The relative flow external to the cylinder in the present experiments consists of a superposition of a vortex and a uniform flow oriented normal to the cylinder axis (caused by motion of the cylinder). The flow due to a stationary vortex alone will lead to separation of the boundary layer after some finite time, even with no cylinder motion. From the computational results reported by Xiao et al.[14] for vortex–cylinder interaction in an otherwise stationary medium, for a case with thickness parameter $T = 18.2$ and vortex Reynolds number $Re_v = 10^6$, the time to separation from impulsive startup of the flow can be estimated as $\Delta t_{sep} = 0.17D^2/\Gamma$. This value increases by about 10% when the vortex Reynolds number is increased to 10^8. For the conditions used in the current experiments, this result implies separation under static conditions, i.e., with no cylinder motion, at $\Delta t_{sep} \cong 0.056$ s. This static separation time is much less than the time required for motion of the cylinder across half of the inner cylindrical tank, which ranges in the experiments from 0.5 to 5.8 s as the cylinder speed is varied. Our results, therefore, indicate that the presence of an ambient normal flow relative to the cylinder acts to significantly delay onset of vortex-induced boundary-layer separation from the cylinder leading edge.

IV. Core Shape Deformation

Computational estimates by Affes and Conlisk[10] indicate that significant inviscid deformation of the vortex core shape may occur as the vortex moves close to the cylinder leading edge. In this section, we examine the extent of core shape deformation and its effect on the cylinder surface pressure distribution by comparing predictions from a computation based on solution of the full Euler equations for a finite-core vortex with predictions from the vortex filament model.

In the former computation, the vortex core is free to deform, whereas in the latter, it is constrained to maintain a circular cross section. The computations are performed for a case with high value of impact parameter ($I = 0.29$) and large cylinder diameter ($D/\sigma_0 = 16.2$), so that boundary-layer separation does not occur until the vortex is very close to the cylinder surface.

The full Euler computation for a deformable vortex is performed using the vorticity collocation method of Marshall and Grant[19] in which the velocity field is obtained by integration of the Biot–Savart integral using a vorticity interpolation in the form of overlapping isotropic Gaussian elements. The element amplitudes are refit at each time step using an iterative procedure.[19] A standard source panel method[17] is used to enforce the no-penetration condition on the cylinder surface, and a multipole acceleration scheme[20] is used to speed up the velocity calculation. The flow is assumed to be periodic in the spanwise direction, which is enforced by including the Biot–Savart integral in three periods of the vorticity field on each side of the computed flow domain. Test computations indicate that inclusion of more than three periods has very little effect on the velocity or pressure fields. The ends of the vortex are connected to buffer regions in which the vorticity field is held fixed and the control points are advected with the freestream velocity U. At the far end of each buffer region, the vortex is joined to a collection of semi-infinite straight vortex filaments, where the number of filaments is set equal to the initial number of control points in the vortex cross section. An expression for the induced velocity from each semi-infinite filament is given by Dhanak.[21]

The numerical algorithm has been validated in test computations by comparison with a variety of exact solutions and by convergence studies in previous papers.[19–22] Validation tests in the current paper, therefore, focus on selection of time step and spatial resolution. Time advancement is performed using a second-order Adams–Bashforth scheme. The time step is held fixed at $\Delta t = 0.1\sigma_0^2/\Gamma$, so that 400 time steps are required for a Lagrangian control point to be advected once around the vortex core. The vortex is discretized using 8750 control points spread over a length of $50\sigma_0$, with 35 points arranged in four concentric circles in each cross section of the vortex tube. Because the focus of this computation is to examine the effect of core shape deformation, the vortex is initially placed fairly close to the cylinder surface (with $S/\sigma_0 = -4$). The cylinder has span length $16\sigma_0$ and diameter $16.2\sigma_0$, and the cylinder surface is discretized using 1672 source panels. The panels are approximately square near the cylinder leading edge, with side length of about $0.4\sigma_0$. Sensitivity to selection of time step and spatial resolution was tested by repeating the computation with approximately half as many (4400) vorticity control points and a time step twice as large ($\Delta t = 0.2\sigma_0^2/\Gamma$). By the end of the computation, the maximum change in the relative vorticity magnitude (change in vorticity magnitude divided by initial vorticity magnitude) predicted in the test computation is within 1.4% of that in the reported computation.

The computation exhibits increasing deformation in shape of the vortex core with time as the cylinder leading edge approaches and passes the initial position of the vortex axis. For instance, the elongated shape of the core is evident in the contour plot of the vorticity magnitude over the vortex cross section in the horizontal symmetry plane shown in Fig. 6 for $S/\sigma_0 = 2.0$. The contour plot is generated by interpolating the computed vorticity values from the Lagrangian control points onto a 101×101 uniform grid with point separation distance of $0.04\sigma_0$. Spanwise and chordwise displacement of the vortex results in stretching of vorticity on the bottom and right-hand sides of the vortex core, respectively. Together with the counterclockwise rotation of the vortex, this stretching results in formation of a backward C-shaped region of high vorticity on the side of the vortex farthest from the cylinder.

Because significant vortex core shape deformation does not occur until the core is quite close to the cylinder surface, the effects of cylinder curvature on the vortex image at this late time may be small. Neglecting curvature effects, a rough estimate of the aspect ratio R of the vortex core at a given closest separation distance d between the vortex axis and the cylinder leading edge is given by the two-dimensional equilibrium solution of Moore and Saffman[23] for a vortex immersed in a straining flow (with straining rate e) as

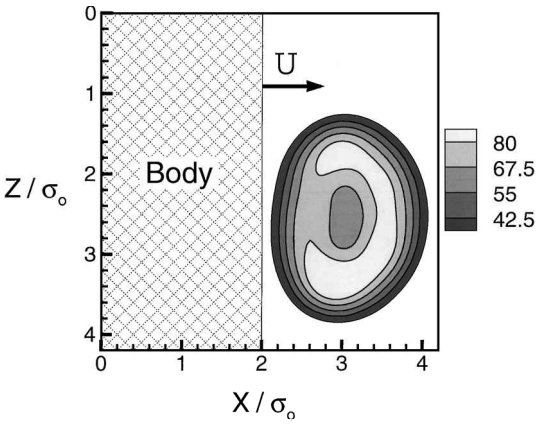

Fig. 6 Vorticity magnitude contour plot for a cross section in the horizontal plane *B*, obtained from an inviscid computation for a case with impact parameter $I = 0.29$ at cylinder position $S/\sigma_0 = 2.0$.

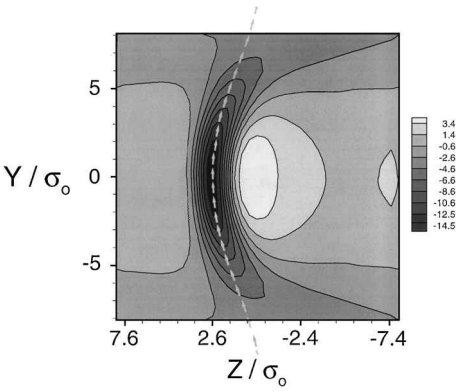

Fig. 7 Contour plot of the relative surface pressure field induced by the vortex on the cylinder surface, projected onto the *x–z* plane, obtained from an inviscid computation at the same time as Fig. 6; vortex axial centerline is indicated by arrows.

$$\frac{e}{\omega} = \frac{R(R-1)}{(R+1)(R^2+1)} \tag{3}$$

The straining rate imposed on the vortex from its image vortex can be estimated using a Taylor series expansion as $e/\omega \cong A/8\pi d^2$, where A is the vortex core area. The aspect ratio predicted from Eq. (3) for a case with $d/\sigma_0 = 1$ (corresponding to the separation distance in Fig. 6) is 1.85, whereas the aspect ratio measured from the isovorticity contours near the core lateral surface in Fig. 6 is approximately 1.5 ± 0.1. Whereas expression (3) appears to overpredict the vortex aspect ratio, it might be useful as a conservative estimate of the extent of core shape deformation in computations with the vortex filament method.

The pressure is computed using the boundary-integral equation approach described by Marshall and Grant.[19] A contour plot of the change in surface pressure from the ambient value (for the cylinder moving through stationary fluid), projected onto the y–z plane, is given in Fig. 7 (for the same time as Fig. 6). The projection of the vortex axial centerline is indicated by arrows. The sense of vortex circulation is such that the lowest velocity on the cylinder surface occurs in the white high-pressure region to the right of the vortex, where the vortex-induced velocity impinges on the cylinder surface. The highest velocity magnitudes are observed to occur directly under the vortex, as indicated by the black low-pressure region. The small high-pressure region on the far-right-hand side of Fig. 7 occurs due to the assumption of periodic boundary conditions along the cylinder span.

To assess the importance of vortex core shape deformation, a comparison of the predicted inviscid slip velocity along the cylinder leading edge for the full Euler computation and for an equivalent (circular) vortex filament is given in Fig. 8. For this comparison, the vortex filament is placed along the geometric centerline of the deformed vortex at the time used in Fig. 6. The predictions for the

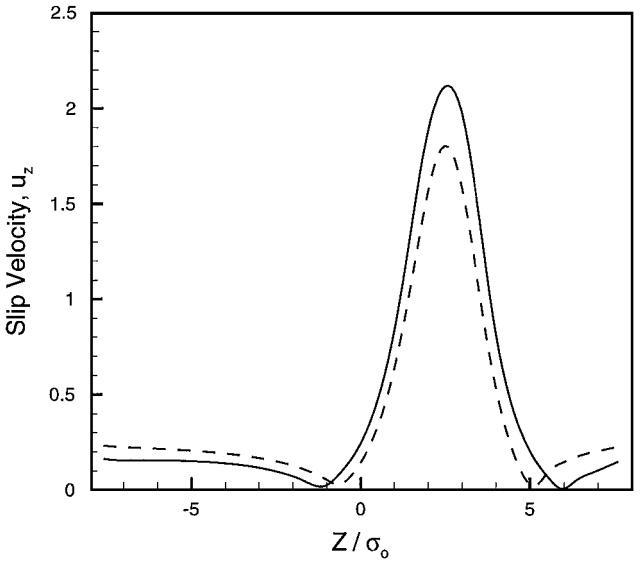

Fig. 8 Comparison of the inviscid slip velocity along the cylinder leading edge, as predicted from a full Euler solution (——) and from a vortex filament model (– – –), at time corresponding to Fig. 6.

fully deformed vortex and the filament are observed to be similar in shape and fairly close in value, with maximum deviation of about 15% at the peak slip velocity. At least for cases where the vortex centerline approaches to a distance of about one core radius σ_0 from the cylinder surface, our results suggest that vortex core shape deformation will not lead to significant errors in prediction of cylinder surface pressure.

V. Topology of Secondary Vorticity Structures

The topology of the secondary vorticity after separation from the cylinder is observed using LIF flow visualization in the horizontal and vertical imaging planes shown in Fig. 1. Volumetric LIF imaging is also performed in the region of vortex–body impact to confirm the topological picture of the secondary vorticity structures suggested by the planar images. The flow visualization study was first performed at high frame rate using the video camera, and select images were obtained using still photography. Cases with $I = 0.21$ and 0.027 are reported as representative of the different secondary vorticity response for high and low values of the impact parameter.

A. High Impact Parameter

For high impact parameters, boundary-layer separation occurs after the vortex has bent considerably about the cylinder surface, such that the distance between the vortex core and the cylinder surface at time of separation is of the order of a core radius. The boundary-layer fluid separates as a sheet along the front surface of the cylinder and wraps around the vortex core. As the secondary vorticity sheet encloses the primary vortex, it is also entrained into the primary vortex core by the self-induced velocity of the secondary vorticity. During this wrapping/entrainment process, both the secondary vortex sheet and the primary vortex become increasingly wavy, followed by rapid disruption of the primary vortex into small-scale turbulence.

An LIF photograph showing the primary vortex interaction with the separated vorticity sheet in a slice of the flow in the vertical plane *A* is given in Fig. 9a. At the time that this photograph is taken, the primary vortex has bent in the spanwise direction by nearly 10 core radii, so that to capture the vortex the vertical imaging plane is translated a distance of 4.5 cm along the cylinder span from the initial position of the vortex axis. A schematic diagram of the secondary vorticity sheet is given in Fig. 9b for this same time, which is based on results obtained from both planar slices and

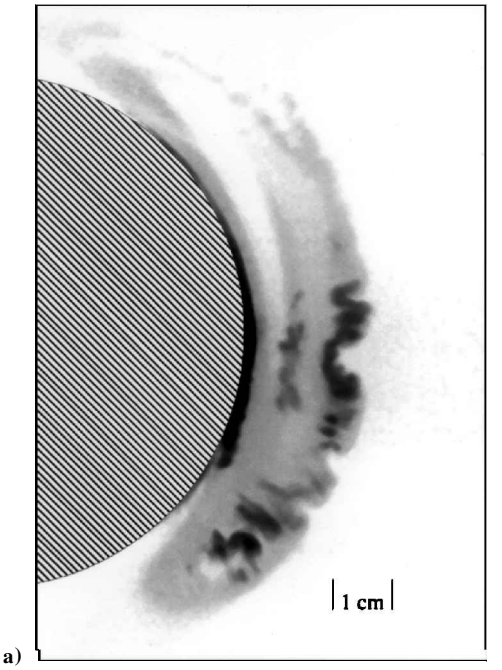

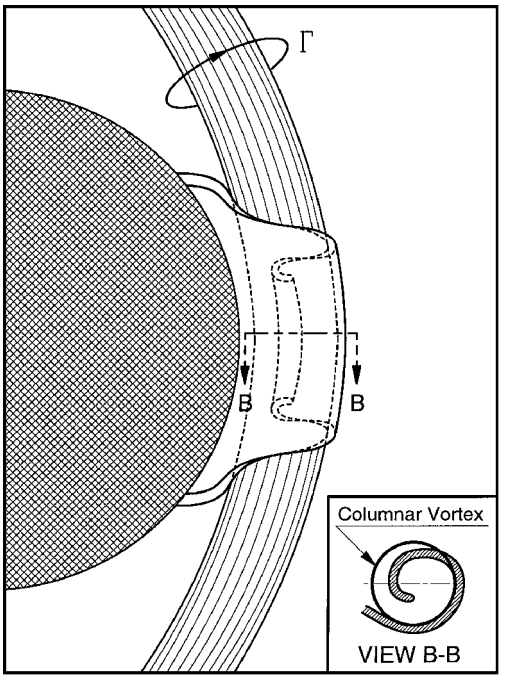

Fig. 9 Wrapping of the separated vorticity sheet (black) about the primary vortex (gray) for a high impact parameter case ($I = 0.21$) with cylinder position $S/\sigma_0 = +11.8$ for a) photograph of an LIF slice in the vertical plane *A* and b) schematic diagram.

volumetric imaging using video pictures. The fluid ejected from the cylinder boundary layer is observed as three dark-colored bands on the vertical imaging plane in Fig. 9a, located on both sides and near the center of the primary vortex (gray). The band on the left is a section of the cylinder boundary layer near the point of ejection from the surface. The band on the right, which is convoluted and wavy, is the secondary vortex sheet in cross section after a half-rotation about the vortex. The band in the center of the primary vortex is the cross section of the secondary vorticity sheet after one full rotation about the vortex. After one rotation, the secondary sheet has become entrained nearly into the center of the primary vortex. Our results indicate that the secondary vorticity maintains an approximately sheet-like form during the first part of its interaction with the primary vortex but that the primary vortex quickly (after one or two rotations of the secondary vortex sheet) breaks up into small-scale turbulence.

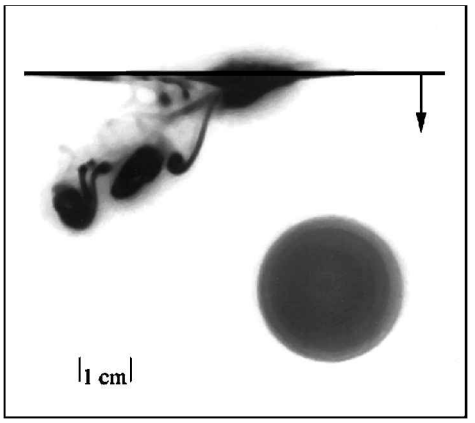

Fig. 10 LIF photograph in the horizontal plane *B* for a low impact parameter case ($I = 0.027$) showing rollup of the separated vorticity sheet at cylinder position $S/\sigma_0 = -8.1$; cylinder leading edge indicated by black line (with arrow to indicate the direction of cylinder motion), and vortex circulation is counterclockwise.

The initial part of the interaction of the primary vortex with the cylinder, therefore, appears to be analogous to the two-dimensional problem of a line vortex near a flat wall, as discussed by Doligalski et al.[4]

B. Low Impact Parameter Case

For low impact parameters, secondary vorticity is ejected away from the cylinder surface as a sheet while the cylinder leading edge is still several core radii away from the vortex. As this vortex sheet is advected away from the cylinder, it gradually develops Kelvin–Helmholtz waves and rolls up to form a series of discrete vortex loops. An LIF photograph showing the rollup of the secondary vorticity sheet shortly after ejection from the body surface in the horizontal plane *B* is given in Fig. 10. The cylinder leading edge is indicated in Fig. 10 by a black line, with an arrow to indicate the direction of cylinder motion. The rollup of the separated vorticity sheet that is observed for cases with low values of the impact parameter may be suppressed at higher impact parameters both because of the shorter time allowed for development of the ejected vortex sheet and because of the effect of stretching in stabilizing the Kelvin–Helmholtz instability.[24]

The interaction of the primary and secondary vorticity is examined in the vertical plane *A*, which is displaced 2 cm along the cylinder span from the initial position of the vortex axis to account for the spanwise bending of the primary vortex. An LIF photograph showing a cross section of the dominant vortex loop somewhat after one full rotation around the primary vortex is given in Fig. 11a, at cylinder position $S/\sigma_0 = -2.0$. A schematic diagram, based on video recordings, is given in Fig. 11b, showing the shape of the secondary vortex loop at the time of the LIF planar slice. The secondary vortex loops are oriented such that they stretch the primary vortex in the region in between the legs of the loops and axially compress the primary vortex outside of this region. This stretching is observed to cause thinning of the primary vortex core near the point at which the loops impinge on the primary vortex and bulging of the primary vortex core both above and below the vortex loops.

In a previous study of vortex interaction with a thin blade, Krishnamoorthy and Marshall[16] observe that the secondary vorticity for that problem also forms loops when the vortex is sufficiently strong. However, for the case of a thin blade, each loop seems to attach directly to the blade boundary layer, and the boundary-layer separation occurs over a wide interval along the blade span. By contrast, in the present experiments the boundary-layer fluid is ejected from the cylinder along a single curve, and the ejected vortex sheet rolls up to form loops at some distance away from the cylinder surface. These differences appear to be due to differences in the nature of boundary-layer separation from the vortex-induced flow off a thin edge compared to a blunt cylinder.

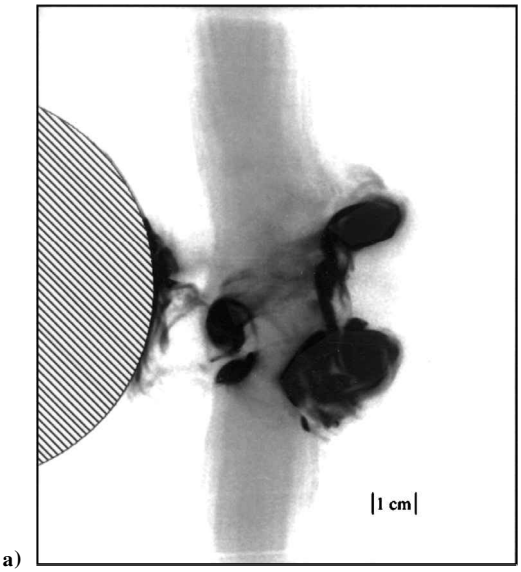

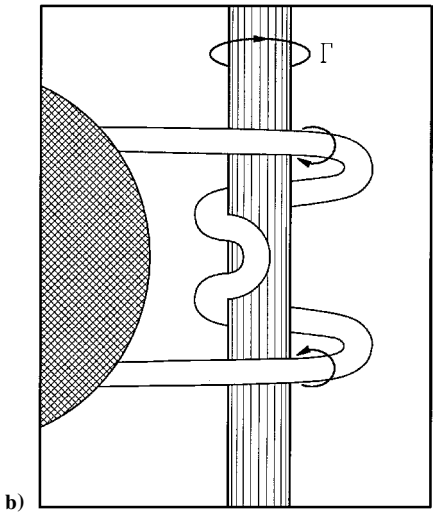

Fig. 11 Secondary vortex loop (black) for a low impact parameter case ($I = 0.027$) as it wraps around the primary vortex (gray) for a) photograph of an LIF slice in the vertical plane *A* with cylinder position $S/\sigma_0 = -2.0$ and b) a schematic diagram.

VI. Conclusions

The results presented will be useful for establishing the practical limitations of inviscid prediction methods for normal vortex interaction with blunt, elongated bodies, of which the cylinder is representative. For the normal vortex–cylinder interaction problem (with no spanwise velocity), it is found that the nature of the cylinder boundary-layer response to the vortex is governed primarily by the impact parameter ($I \equiv 2\pi\sigma_0 U/\Gamma$), which represents the ratio of the vortex–cylinder impact velocity to the maximum vortex swirl velocity. For high values of impact parameter, boundary-layer separation occurs very late, after the vortex has wrapped around the cylinder surface and has become deformed in both core position and cross-sectional shape. For low values of impact parameter, boundary-layer separation occurs very early, before the vortex has had time to respond much to the presence of the cylinder. The paper examines the nature of the secondary vorticity response and the applicability of inviscid vortex filament prediction methods over a range of impact parameters that encompass these two extremes.

Data for the onset of vortex-induced boundary-layer separation from the cylinder leading edge indicate that motion of the cylinder toward the vortex plays an important role in delaying onset of vortex-induced boundary-layer separation from the cylinder leading edge. The cylinder position at separation onset is very sensitive to impact parameter for $I < 0.08$ but becomes less sensitive to impact parameter for $I > 0.2$. Experimental data for vortex displacement

both before and after separation are compared to predictions of the vortex filament model for different impact parameters. The vortex displacement data are observed to continue the trend predicted by inviscid theory for some time interval following separation, during which time the secondary vorticity structures are advected away from the cylinder surface and carried closer to the primary vortex. At high impact parameters, breakup of the vortex occurs rapidly after separation, and the secondary vorticity has little chance to modify the vortex position. At low impact parameters, a point is reached where the displacement data deviate sharply from the filament model predictions due to the velocity induced by the secondary vorticity structures.

The effect of deformation of vortex core cross-sectional shape is evaluated by comparing the surface slip velocity on the cylinder leading edge for a deformed vortex with aspect ratio 1.5, as predicted by a computation using the full Euler equation, with predictions of a vortex filament model. The extent of vortex core shape deformation is found to be less than predicted by a simple two-dimensional model, and the shape deformation is observed to have little effect on the predicted inviscid surface slip velocity.

The topology of the secondary vorticity is found to be qualitatively different for cases with high and low values of the impact parameter. For all cases examined, the boundary layer seems to separate from the cylinder leading edge in a sheet-like form. For low values of the impact parameter, the separated vorticity sheet becomes unstable and rolls up to form a series of discrete vortex loops. These vortex loops subsequently wrap around and become entrained into the primary vortex core. The stretching induced by the legs of the loops induces thinning of the primary vortex core near the point of loop impact, formation of bulging waves on the vortex core both above and below the loops, and ejection of fluid from the primary vortex core. For high values of the impact parameter, the vortex is very close to the cylinder surface at the time of boundary-layer separation, and the separated vorticity sheet appears to wrap around and become entrained into the vortex core without undergoing the rollup process. The primary vortex quickly disrupts into small-scale turbulence in the high impact parameter case after one or two rotations of the secondary vortex sheet.

Acknowledgments

This research was supported by funding from the U.S. Army Research Office under Grant DAAH04-96-1-0081 to the University of Iowa. Thomas L. Doligalski is the Program Manager. Computer time was provided by a grant from the San Diego Supercomputing Center.

References

[1]Sheridan, P. F., and Smith, R. P., "Interactional Aerodynamics—A New Challenge to Helicopter Technology," *Journal of the American Helicopter Society*, Vol. 25, No. 1, 1980, pp. 3–21.

[2]Conlisk, A. T., "Modern Helicopter Aerodynamics," *Annual Review of Fluid Mechanics*, Vol. 29, 1997, pp. 515–567.

[3]Rockwell, D., "Vortex-Body Interactions," *Annual Review of Fluid Mechanics*, Vol. 30, 1998, pp. 199–229.

[4]Doligalski, T. L., Smith, C. R., and Walker, J. D. A., "Vortex Interaction with Walls," *Annual Review of Fluid Mechanics*, Vol. 26, 1994, pp. 573–616.

[5]Kim, J. M., and Komerath, N. M., "Summary of the Interaction of a Rotor Wake with a Circular Cylinder," *AIAA Journal*, Vol. 33, No. 3, 1995, pp. 470–478.

[6]Liou, S. G., Komerath, N. M., and McMahon, H. M., "Measurement of the Interaction Between a Rotor Tip Vortex and a Cylinder," *AIAA Journal*, Vol. 28, No. 6, 1990, pp. 975–981.

[7]Bi, N., Leishman, J. G., and Crouse, G. L., "Investigation of Rotor Tip Vortex Interaction with a Body," *Journal of Aircraft*, Vol. 30, No. 6, 1993, pp. 879–888.

[8]Brand, A., Komerath, N. M., and McMahon, H., "Results from Laser Sheet Visualization of a Periodic Rotor Wake," *Journal of Aircraft*, Vol. 26, No. 5, 1989, pp. 438–443.

[9]Brand, A. G., Komerath, N. M., and McMahon, H. M., "Correlations of Rotor Wake/Airframe Interaction Measurements with Flow Visualization Data," *Journal of the American Helicopter Society*, Vol. 10, 1990, pp. 4–15.

[10]Affes, H., and Conlisk, A. T., "Model for Rotor Tip Vortex–Airframe Interaction Part 1: Theory," *AIAA Journal*, Vol. 31, No. 12, 1993, pp. 2263–2273.

[11]Affes, H., Conlisk, A. T., Kim, J. M., and Komerath, N. M., "Model for Rotor Tip Vortex-Airframe Interaction, Part 2: Comparison with Experiment," *AIAA Journal*, Vol. 31, No. 12, 1993, pp. 2274–2282.

[12]Marshall, J. S., and Yalamanchili, R., "Vortex Cutting by a Blade, Part II: Computations of Vortex Response," *AIAA Journal*, Vol. 32, No. 7, 1994, pp. 1428–1436.

[13]Affes, H., Xiao, Z., and Conlisk, A. T., "The Boundary-Layer Flow Due to a Vortex Approaching a Cylinder," *Journal of Fluid Mechanics*, Vol. 275, 1994, pp. 33–57.

[14]Xiao, Z., Burggraf, O. R., and Conlisk, A. T., "The Interacting Boundary-Layer Flow Due to a Vortex Approaching a Cylinder," *Journal of Fluid Mechanics*, Vol. 346, 1997, pp. 319–343.

[15]Affes, H., Xiao, Z., Conlisk, A. T., Kim, J. M., and Komerath, N. M., "Model for Rotor Tip Vortex–Airframe Interaction Part 3: Viscous Flow on Airframe," *AIAA Journal*, Vol. 36, No. 3, 1998, pp. 409–415.

[16]Krishnamoorthy, S., and Marshall, J. S., "Three-Dimensional Blade–Vortex Interaction in the Strong Vortex Regime," *Physics of Fluids*, Vol. 10, No. 11, 1998, pp. 2828–2845.

[17]Hess, J. L., and Smith, A. M. O., "Calculation of Potential Flow About Arbitrary Bodies," *Progress in Aeronautical Sciences*, Vol. 8, 1966, pp. 1–138.

[18]Knio, O. M., and Ghoniem, A. F., "Numerical Study of a Three-Dimensional Vortex Method," *Journal of Computational Physics*, Vol. 86, No. 1, 1990, pp. 75–106.

[19]Marshall, J. S., and Grant, J. R., "Penetration of a Blade into a Vortex Core: Vorticity Response and Unsteady Blade Forces," *Journal of Fluid Mechanics*, Vol. 103, 1996, pp. 83–109.

[20]Greengard, L., and Rokhlin, V., "A Fast Algorithm for Particle Simulations," *Journal of Computational Physics*, Vol. 73, 1987, pp. 325–348.

[21]Dhanak, M. R., "Interaction Between a Vortex Filament and an Approaching Rigid Sphere," *Journal of Fluid Mechanics*, Vol. 110, 1981, pp. 129–147.

[22]Marshall, J. S., and Grant, J. R., "A Lagrangian Vorticity Collocation Method for Viscous, Axisymmetric Flows with and Without Swirl," *Journal of Computational Physics*, Vol. 138, 1997, pp. 302–330.

[23]Moore, D. W., and Saffman, P. G., "Structure of a Line Vortex in an Imposed Strain," *Aircraft Wake Turbulence and Its Detection*, Plenum, New York, 1971, pp. 339–354.

[24]Moore, D. W., and Griffith-Jones, R., "The Stability of an Expanding Circular Vortex Sheet," *Mathematika*, Vol. 21, 1974, pp. 128–133.

A. Plotkin
Associate Editor